AGU PUBLICATIONS

JGR

Journal of Geophysical Research: Oceans

RESEARCH ARTICLE

10.1002/2016JC012331

Key Points:
- Internal gravity waves and nonstationary internal tides have nonnegligible sea surface height signatures
- High-resolution global ocean models are beginning to resolve the internal gravity wave continuum
- Internal gravity waves and nonstationary internal tides may cause contamination in upcoming satellite altimeter missions

Correspondence to:
A. C. Savage,
savagea@umich.edu

Citation:
Savage, A. C., et al., (2017), Frequency content of sea surface height variability from internal gravity waves to mesoscale eddies, *J. Geophys. Res. Oceans*, *122*, 2519–2538, doi:10.1002/2016JC012331.

Received 12 SEP 2016
Accepted 28 FEB 2017
Accepted article online 2 MAR 2017
Published online 28 MAR 2017

Frequency content of sea surface height variability from internal gravity waves to mesoscale eddies

Anna C. Savage[1], Brian K. Arbic[2], James G. Richman[3], Jay F. Shriver[4], Matthew H. Alford[5], Maarten C. Buijsman[6], J. Thomas Farrar[7], Hari Sharma[8], Gunnar Voet[5], Alan J. Wallcraft[4], and Luis Zamudio[3]

[1]Applied Physics Program, University of Michigan, Ann Arbor, Michigan, USA, [2]Department of Earth and Environmental Sciences, University of Michigan, Ann Arbor, Michigan, USA, [3]Center for Oceanic-Atmospheric Prediction Studies, Florida State University, Tallahassee, Florida, USA, [4]Oceanography Division, Naval Research Laboratory, Stennis Space Center, Mississippi, USA, [5]Scripps Institution of Oceanography, University of California, San Diego, La Jolla, California, USA, [6]Department of Marine Sciences, University of Southern Mississippi, Hattiesburg, Mississippi, USA, [7]Phyical Oceanography Department, Woods Hole Oceanographic Institution, Woods Hole, Massachusetts, USA, [8]Portage Northern High School, Portage, Michigan, USA

Abstract High horizontal-resolution (1/12.5° and 1/25°) 41-layer global simulations of the HYbrid Coordinate Ocean Model (HYCOM), forced by both atmospheric fields and the astronomical tidal potential, are used to construct global maps of sea surface height (SSH) variability. The HYCOM output is separated into steric and nonsteric and into subtidal, diurnal, semidiurnal, and supertidal frequency bands. The model SSH output is compared to two data sets that offer some geographical coverage and that also cover a wide range of frequencies—a set of 351 tide gauges that measure full SSH and a set of 14 in situ vertical profilers from which steric SSH can be calculated. Three of the global maps are of interest in planning for the upcoming Surface Water and Ocean Topography (SWOT) two-dimensional swath altimeter mission: (1) maps of the total and (2) nonstationary internal tidal signal (the latter calculated after removing the stationary internal tidal signal via harmonic analysis), with an average variance of 1.05 and 0.43 cm^2, respectively, for the semidiurnal band, and (3) a map of the steric supertidal contributions, which are dominated by the internal gravity wave continuum, with an average variance of 0.15 cm^2. Stationary internal tides (which are predictable), nonstationary internal tides (which will be harder to predict), and nontidal internal gravity waves (which will be very difficult to predict) may all be important sources of high-frequency "noise" that could mask lower frequency phenomena in SSH measurements made by the SWOT mission.

1. Introduction

Sea surface height (SSH) is a complicated manifestation of many processes both within and at the surface of the ocean and, as such, is difficult to observe and model over a wide range of space and time scales. The two instruments primarily used to observe SSH are satellite altimeters and tide gauges. Satellite altimetry, which provides near-global coverage, is an invaluable tool in the study of the global ocean [*Fu and Cazenave*, 2001]. However, the long repeat periods (ranging from several days to months) of altimeters alias high-frequency motions. Tide gauges, another invaluable tool for oceanographers, suffer from the opposite problem. While most tide gauges record measurements every hour, tide gauge networks offer limited spatial coverage, particularly in the deep ocean, due to the continental coastal locations of many tide gauges. Many studies have used tide gauges in tandem with altimeter data. For example, *Wunsch* [1991] used both types of data to examine global SSH variability, and *Ray and Mitchum* [1997] used tide gauges and altimetry to examine internal tides. Here we complement the literature on SSH variance in altimetry and tide gauges with an examination of SSH output in two new global simulations of the HYbrid Coordinate Ocean Model (HYCOM) [*Chassignet et al.*, 2009]. The new HYCOM simulations are forced by both tidal and atmospheric fields [*Arbic et al.*, 2010, 2012; *Shriver et al.*, 2014; *Ansong et al.*, 2015; *Buijsman et al.*, 2016; *Ngodock et al.*, 2016] and therefore have the potential to realistically simulate SSH variance on a global scale over periods from hours to years. As a hybrid coordinate model, HYCOM also has the potential to accurately model both coastal and open-ocean sea level variance. To qualitatively validate model

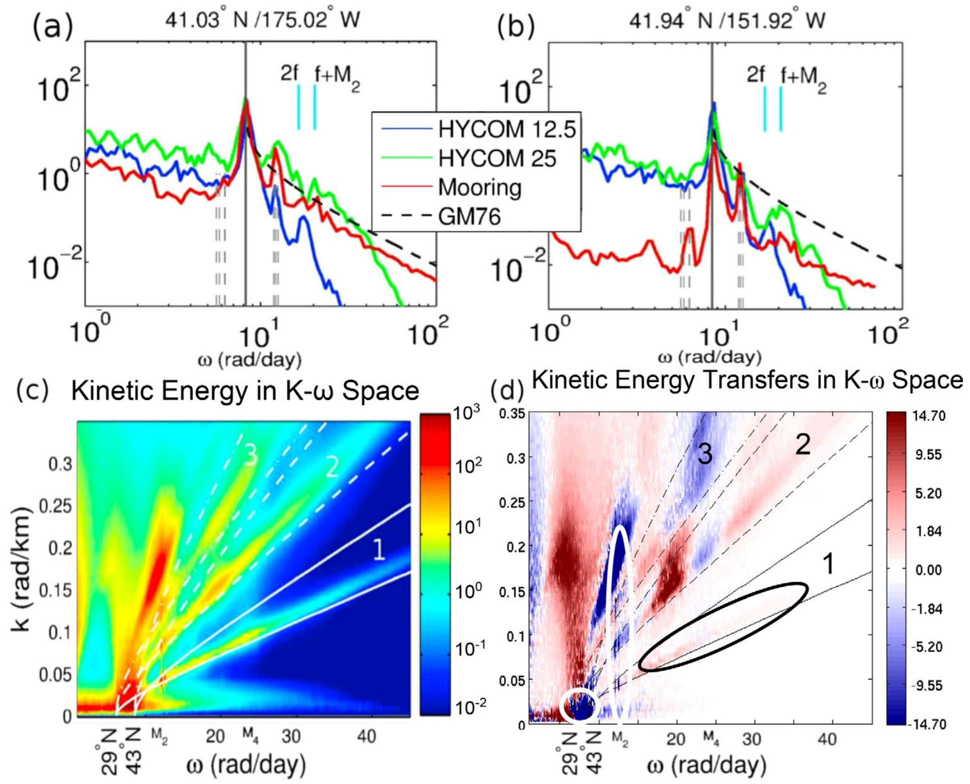

Figure 1. Adapted from *Müller et al*. [2015]. (a and b) Frequency spectral density of surface kinetic energy $[(m/s)^2(d)]$ from 1/12.5° and 1/25° HYCOM (HYCOM12 and HYCOM25, respectively) at two sample North Pacific mooring locations (coordinates given in subplot titles). The mooring spectral density and spectral density from *Garrett and Munk* [1975], GM76, are also given; see *Müller et al*. [2015] for details of the GM76 spectra. (c) Surface kinetic energy wave number-frequency spectral density $[(m/s)^2(d)(km)]$ computed from HYCOM25 in a box in the North Pacific. High variance is seen along the theoretical wave number-frequency slopes for vertical modes. First mode is represented by a solid white curves, second mode by a dashed white curves, and third mode by a dotted-dashed white curves. (d) Kinetic energy transfers $[(10^{-9}W/kg)(d)(km)]$ computed from HYCOM25 in frequency-wave number space. Blue (negative) values represent energy being removed from the system while red represent energy injection. See text for description of regions highlighted with ellipses.

accuracy in both coastal and open-ocean regions, we compare model output to tide gauge and in situ depth-profiling observations.

In this study, we focus on SSH frequency spectral densities, which have been computed from tide gauges and altimeter data in multiple studies [*Pattiaratchi and Wijeratne*, 2009; *Wunsch and Stammer*, 1995; *Ray*, 1998; *Colosi and Munk*, 2006; *Wunsch*, 2010]. We divide the HYCOM SSH output into steric and nonsteric components, where steric SSH arises from baroclinic motions (e.g., fronts, eddies, thermal expansion, and internal gravity waves including internal tides) and nonsteric SSH arises from mass changes in the water column (e.g., barotropic tides, pressure- and wind-forced barotropic variability) [*Baker-Yeboah et al*., 2009]. We compare the frequency spectral densities of full (steric plus nonsteric) SSH in HYCOM and 351 tide gauges in a global database, and the frequency spectral densities of steric SSH in HYCOM and 14 in situ depth-profiling instruments. The steric SSH can be computed from any in situ instrument that measures temperature and salinity over a significant fraction of the water column, especially the upper ocean. Examples of the latter approach include steric SSH computed from ARGO floats [*Roemmich and Owens*, 2000] and steric SSH calculations made from moored instruments [*Zantopp and Leaman*, 1984]. The small number of in situ depth-profiling instruments used here feature high-frequency sampling in time as well as high vertical resolution, thus enabling a model-data comparison of steric SSH over tidal and supertidal bands. The tide gauge and in situ vertical profiler data sets we use here are the only observational data sets we are aware of that offer a wide (quasi-global, in the case of the tide gauges) geographical coverage at the same time that they cover a wide range of frequencies. For this reason, we compare our model to both tide gauge and in situ vertical profiler data sets, while being fully aware that the two data sets are rather distinct. The 351 tide

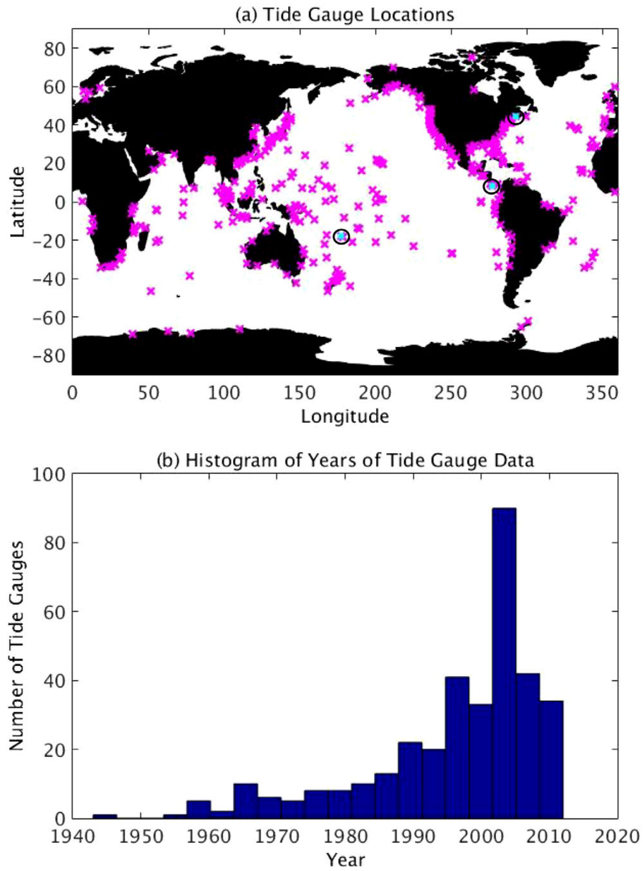

Figure 2. (a) Map of 351 tide gauges used in comparison of full (steric plus nonsteric) SSH variance with HYCOM results. The locations marked with the filled cyan squares (circled in black for emphasis) are used for comparison in Figure 5. Longitude (latitude) is measured in degrees north (east) in Figures 2, 3, and 7. All tide gauges are in the University of Hawai'i Sea Level Center (UHSLC) database. Only gauges with 1 year of continuous hourly data are used here. (b) Histogram of years of data collected from the UHSLC tide gauge database.

gauges measure full SSH in locations that are primarily continental coastal, whereas the in situ vertical profilers measure salinity and temperature from which we calculate steric SSH in 14 open-ocean locations.

We integrate the frequency spectral densities over four frequency bands that are associated with specific physical processes. The division of the modeled spectral densities into steric and nonsteric components also aids in associating the SSH variability with physical processes. For instance, mesoscale eddies and western boundary currents dominate subtidal steric SSH variability [*Le Traon and Morrow*, 2001]. Atmospheric pressure loading and winds contribute importantly to nonsteric SSH variance over a wide range of frequencies, from supertidal to annual and longer [*Ponte and Gaspar*, 1999; *Shriver and Hurlburt*, 2000; *Stammer et al*., 2000; *Tierney et al*., 2000; *Carrère and Lyard*, 2003; *Fu and Cazenave*, 2001]. Diurnal and semidiurnal barotropic tides contribute importantly to nonsteric SSH [*Le Provost*, 2001] and diurnal and semidiurnal internal tides contribute importantly to steric SSH variance [*Ray and Mitchum*, 1997; *Ray and Zaron*, 2016; *Shriver et al*., 2012]. Finally, the internal gravity wave continuum contributes to the steric supertidal SSH variance [*Glazman and Cheng*, 1999].

A major focus of this study is the steric SSH variability due to stationary internal tides, nonstationary internal tides, and the internal gravity wave (IGW) continuum. There is growing interest in the satellite altimeter community in the SSH signatures of internal tides and the IGW continuum, particularly because internal tides and IGWs have significant variance at high wave numbers [*Richman et al*., 2012; *Callies and Ferrari*, 2013; *Rocha et al*., 2016]. These high wave numbers are targeted for study by planned two-dimensional swath altimeter missions [*Fu et al*., 2012]. Several previous studies have developed empirical maps of stationary internal tides [*Dushaw et al*., 2011; *Ray and Zaron*, 2016; *Zhao et al*., 2016]. Because the nonstationary internal tides and the IGW continuum are less predictable than the stationary internal tides, they may represent an even greater challenge to the altimetry community. We take a step toward understanding this challenge by producing global maps of the geographical variability of nonstationary and stationary internal tides and the IGW continuum. Internal tides and waves are also of interest to the oceanography community because the mixing associated with internal wave breaking may exert a control on the oceanic meridional overturning circulation [*Munk and Wunsch*, 1998; *Ferrari and Wunsch*, 2009].

In our examination of supertidal steric SSH, we build upon work done in *Müller et al*. [2015], which showed that high-resolution simulations that are forced by both atmospheric fields and tides begin to develop an IGW continuum. Figure 1 encapsulates results from *Müller et al*. [2015]. In *Müller et al*. [2015], two earlier HYCOM simulations were compared against an array of moorings in the North Pacific. Figures 1a and 1b show frequency spectral densities of surface kinetic energy computed from $1/12.5^\circ$ and $1/25^\circ$ simulations of HYCOM, and from a mooring, against the Garrett-Munk spectral slope for internal waves [*Garrett and*

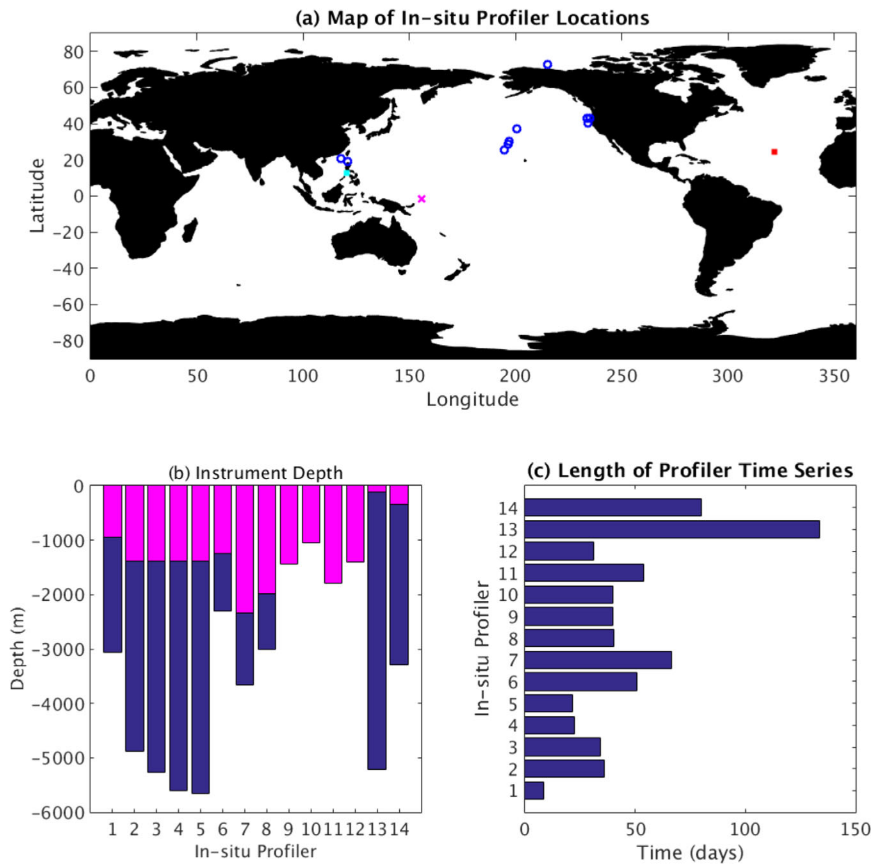

Figure 3. (a) Locations of 14 in situ profilers used to compare steric SSH variance with HYCOM results. The locations marked with the filled cyan and red squares are used for example steric SSH frequency spectral density comparisons (Figures 8a and 8b, respectively). The blue circles represent the remaining McLane profiler locations, and the pink cross marks the location of the other surface mooring. (b) Maximum depth used in calculation of steric SSH from both in situ instrument and HYCOM output (pink) compared to full depth of water column at location of instrument (blue). (c) Length of time series used in calculation of steric SSH frequency spectral densities for each in situ profiling instrument.

Munk, 1975]. The moorings most closely match the theoretical slope. The spectral density of the $1/12.5^\circ$ HYCOM simulation falls off much more quickly at the high-frequencies than the spectral density of the $1/25^\circ$ HYCOM simulation, which therefore matches the observed spectral densities much better at higher frequency in both locations. Figure 1c shows kinetic energy frequency-horizontal wave number spectral density computed from a box in the North Pacific in $1/25^\circ$ HYCOM. The white curves represent the linear dispersion relation curves for internal gravity waves, computed from the Sturm-Liouville equation for vertical modes at the northern and southern most latitudes of the North Pacific box in order to bound the modal peaks. The first three vertical modes are shown. There are peaks at the inertial and semidiurnal bands, and significant energy along the linear dispersion relation curves for IGWs, the latter in accordance with the notion that an IGW spectrum is developing. Finally, Figure 1d shows the nonlinear kinetic energy transfers in frequency-horizontal wave number space from $1/25^\circ$ HYCOM. The negative values, shown in blue, indicate where the nonlinear transfers remove energy, and the positive values, shown in red, show where the nonlinearities inject energy into the system. It is clear from Figure 1d that energy is being removed from inertial and tidal frequencies (indicated with white ellipses) and added at supertidal frequencies along the linear dispersion curves for internal waves, particularly the first mode dispersion curve (indicated with a black ellipse). In summary, Figure 1 demonstrates that high-resolution general circulation global ocean models with tidal and atmospheric forcing, such as the HYCOM simulations studied here, are beginning to resolve the IGW continuum.

After describing our HYCOM simulations, observational data, and methodology, we compare frequency spectral energy densities of full SSH in HYCOM versus tide gauges and of steric SSH in HYCOM versus in situ

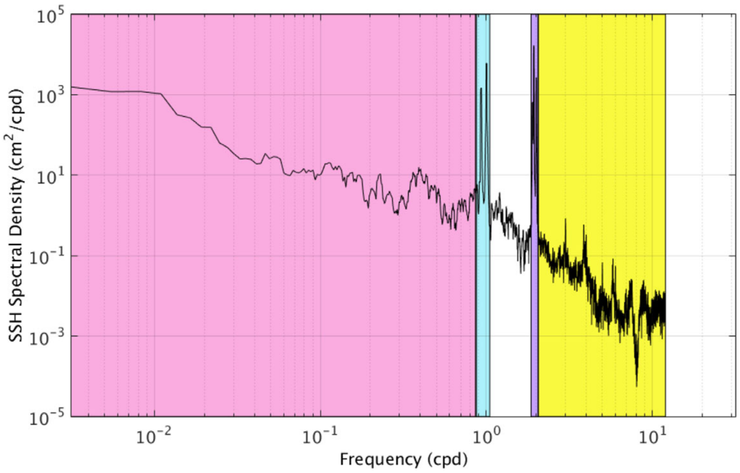

Figure 4. Example frequency spectral density from HYCOM25 near Hilo, Hawai'i (204.96°E, 19.70°N) with colors shading the frequency bands used in making global maps of SSH variance. The pink region represents the subtidal band, the teal region is the diurnal band, the purple region is the semidiurnal band, and the yellow region represents the supertidal band.

depth-profiling instruments. We then create global maps of steric and nonsteric SSH variance, integrated over different frequency bands, in 1/12.5° and 1/25° HYCOM. The comparison of the IGW continuum in HYCOM and observations, and the comparison of 1/12.5° and 1/25° resolution HYCOM, informs us about whether a numerical convergence has been reached, or whether the continuum estimates shown here represent a lower bound. The variance is integrated over four bands: subtidal, two tidal bands (diurnal and semidiurnal), and supertidal. The supertidal steric SSH is assumed to be dominated by the IGW continuum. Motivated by the interest in nonstationary tides, the integrals of the diurnal and semidiurnal SSH frequency spectral densities are computed before and after the stationary part of the tides are removed. The global maps of nonstationary internal tidal and IGW continuum SSH variance are of consequence for the upcoming Surface Water and Ocean Topography (SWOT) satellite altimeter mission [*Fu et al*., 2012], which will measure SSH in two-dimensional swaths, allowing for unprecedented global coverage. In this study, we will show that HYCOM is reasonably well matched to data across all frequencies, and will use its global coverage to examine and map SSH contributions from a variety of frequency bands.

2. HYCOM Simulations, Observations, and Methodology

2.1. HYCOM Simulations

The HYCOM simulations used in this study are forced by the astronomical tidal potential [*Cartwright*, 1999] of the three largest semidiurnal constituents (M_2, S_2, and N_2) and the two largest diurnal constituents (K_1 and O_1). The simulations use a topographic wave drag field, taken from *Jayne and St. Laurent* [2001], and tuned to minimize barotropic tidal errors with respect to the altimeter-constrained tide model TPXO [*Egbert et al*., 1994]. The tuning is described in *Buijsman et al*. [2015]. The impacts of the wave drag in damping the barotropic and baroclinic tides are described in *Ansong et al*. [2015] and the impacts of the wave drag on the model barotropic and baroclinic tidal energy budget are described in *Buijsman et al*. [2016]. The HYCOM simulations have 41 layers in the vertical direction, a 1/12.5° horizontal resolution (~8 km) in one simulation, and a 1/25° horizontal resolution (~4 km) in the second simulation. Throughout this paper, we will refer to these simulations as HYCOM12 and HYCOM25, respectively. Wave drag tuning was performed for HYCOM12, but, due to the high computational costs of such simulations, was not redone for HYCOM25. Hence, the wave drag in the HYCOM25 simulation may be less than optimal in some respects. Atmospheric pressure, wind, and buoyancy forcing is taken from the U.S. Navy Global Environmental Model, NAVGEM [*Hogan et al*., 2014]. NAVGEM is run on a 37 km grid, and interpolated to a 0.5° application grid used to force both HYCOM simulations. HYCOM12 is forced hourly by NAVGEM while HYCOM25 is forced every 3 hours. In both HYCOM simulations, an Augmented State Ensemble Kalman Filter is employed to reduce the global M_2 barotropic tidal errors [*Ngodock et al*., 2016], averaged over waters deeper than 1000 m to about 2.6 cm compared to the altimeter-constrained model TPXO [*Egbert et al*., 1994]. General details about HYCOM can be found in *Chassignet et al*. [2009] and *Metzger et al*. [2010]. We use hourly HYCOM SSH output saved over 1 year. The 1 year duration of HYCOM output is dictated by the very large computational and storage costs associated with such high-resolution ocean models. HYCOM12 output is saved from November 2011 to October 2012, while HYCOM25 is saved from January 2014 to December 2014. The steric SSH put out by HYCOM is computed as outlined in Appendix A. The nonsteric SSH is computed as the difference

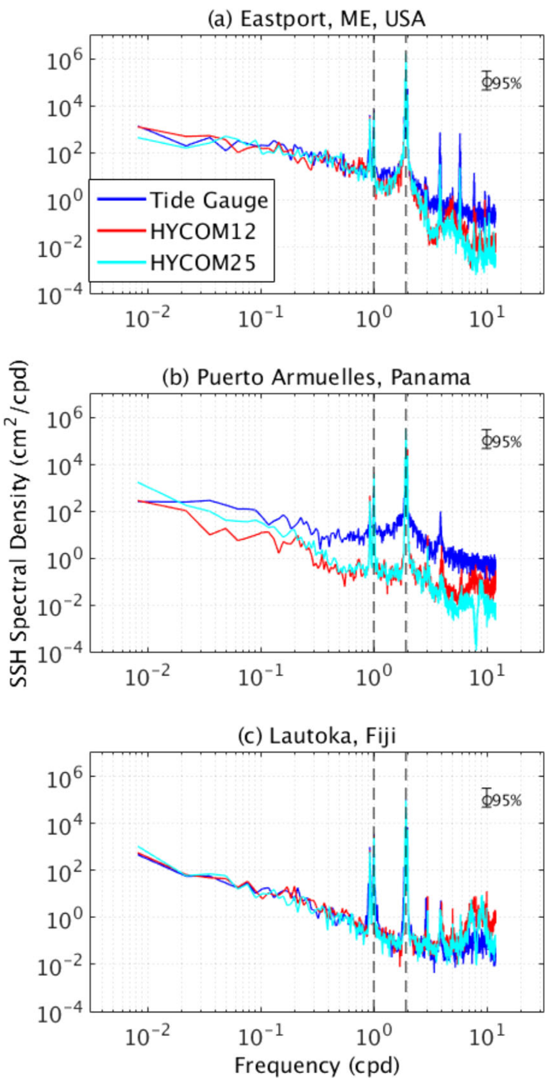

Figure 5. Example SSH frequency spectral densities of tide gauge data and corresponding model grid point output in (a) Eastport, Maine, (b) Puerto Armuelles, Panama, and (c) Lautoka, Fiji. Dashed lines denote K_1 diurnal and M_2 semidiurnal tidal frequencies. The 95% confidence interval shown accounts only for random error in spectral density calculations.

between full and steric SSH. We have found that the method of computing steric SSH in HYCOM produces spectral densities essentially identical to those computed from steric height calculated in the more traditional way, to be given in equation (1). The HYCOM outputs of steric and nonsteric SSH are used in constructing global maps of SSH variance in different frequency bands.

2.2. Tide Gauge Data

The tide gauge data are taken from the University of Hawai'i Sea Level Center (UHSLC) tide gauge database [*Caldwell et al.*, 2011]. We use hourly tide gauge data, to match the hourly HYCOM output. For each tide gauge, 1 year of continuous data are extracted from the UHSLC database. The HYCOM output used for comparison with the tide gauges is taken at the nearest neighbor model grid points corresponding to the tide gauge locations. The 1 year time period is dictated by the duration of available tide gauge records in the UHSLC database as well as the duration of available HYCOM output. Out of almost 1000 tide gauges in the UHSLC database, 351 tide gauge locations meet our criteria of having 1 year of continuous hourly output. A map of the 351 locations is given in Figure 2a. As seen in Figure 2a, there is a noticeable continental coastal bias in the tide gauge locations. A histogram of the years covered by the tide gauge data is shown in Figure 2b. The majority of the tide gauges used cover years in the 21st century.

2.3. In Situ Depth-Profiling Data

We use in situ instrument depth-profiling data at 14 locations where high-frequency and high vertical-resolution temperature and salinity data are available to compute frequency spectral densities of steric sea surface height in the tidal and supertidal bands. Because high-frequency steric SSH variability can only be considered to be representative of the internal gravity wave continuum in deep water, only moorings that are in more than 1000 m of water are used for this comparison. A map of the 14 in situ profiler locations is given in Figure 3a, while Figure 3b shows the depths of each instrument and Figure 3c shows the length of the time series from each profiler. At locations 13 and 14 in Figures 3b and 3c, we have data from surface moorings [*Farrar et al.*, 2015; *Weller and Anderson*, 1996]. Because the temperature is sampled at higher vertical resolution in the surface moorings than the salinity, the salinity is interpolated to the temperature measurement depths. As these measurement depths are not evenly separated, a trapezoidal integration technique is used in the steric sea surface height calculation. The sampling intervals are approximately 1 hour, and vary by instrument. Record durations from these two surface moorings are approximately 75 and 130 days. In the other 12 locations (locations 1–12 in Figures 3b and 3c), McLane profilers are used [*Doherty et al.*, 1999]. The temperature and salinity data are sampled coincidentally and are mapped onto 2 db intervals. The sampling period is also approximately 1 hour, varying by instrument. Record durations of the McLane profilers range from eight days to two months, as seen in Figure 3c. Due to the uneven temporal sampling of both surface moorings and McLane profilers,

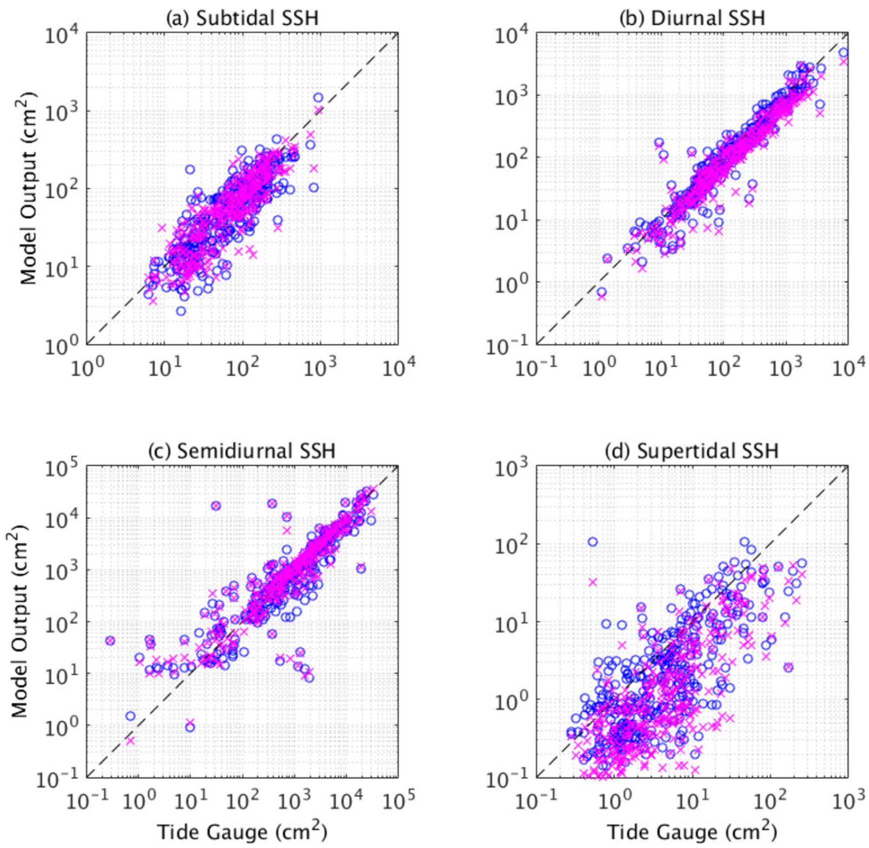

Figure 6. Scatterplot of full SSH variance (cm^2) in model output versus tide gauge data in (a) subtidal, (b) diurnal, (c) semidiurnal, and (d) supertidal frequency bands. Axis limits differ between subplots.

both sets of data are interpolated in time to even 1 hour sampling intervals in order to allow for spectral energy densities to be computed.

Time series of steric height are computed from in situ profiler data using the standard definition [*Knauss*, 1997] given as

$$h(p_1, p_2) = \frac{1}{g}\int_{p_1}^{p_2} \alpha(S, T, p)dp \quad (1)$$

where S, T, and p denote salinity, temperature, and pressure, respectively, and $\alpha(S, T, p)$ is the specific volume, defined as $1/\rho$, where ρ is density. Division by the gravitational acceleration, g, ensures correct units of height, $h(p_1, p_2)$, where p_1 and p_2 are the integration bounds. The steric height was computed over the upper ocean depth intervals for which data were collected. The HYCOM steric SSH values used in the model-data comparisons are computed over the same depths as the corresponding instrument using equation (1). The average number of pressure levels used in the integration for steric SSH for each profiling instrument is $\sim$477, while the average number of pressure levels used for integration in HYCOM is $\sim$31 pressure levels. Figure 3b shows the maximum depth of each instrument, shown in pink, over the full depth of the water column at the instrument location, shown in blue. Although the surface moorings do not cover as much of the water column as the McLane profilers (Figure 3b), the two surface moorings have the longest time series of the in situ instruments (Figure 3c). This illustrates the unfortunate trade-off between high vertical sampling and long time series with such data. Because the McLane profiler data records are of short duration, we omit the subtidal band from our comparison of HYCOM and in situ profiler data.

2.4. Methodology

Before frequency spectral densities are computed, both a linear trend and a mean are removed from each SSH time series, *SSH*(*t*). Following this, each time series is multiplied by a Tukey window having a ratio of taper-to-

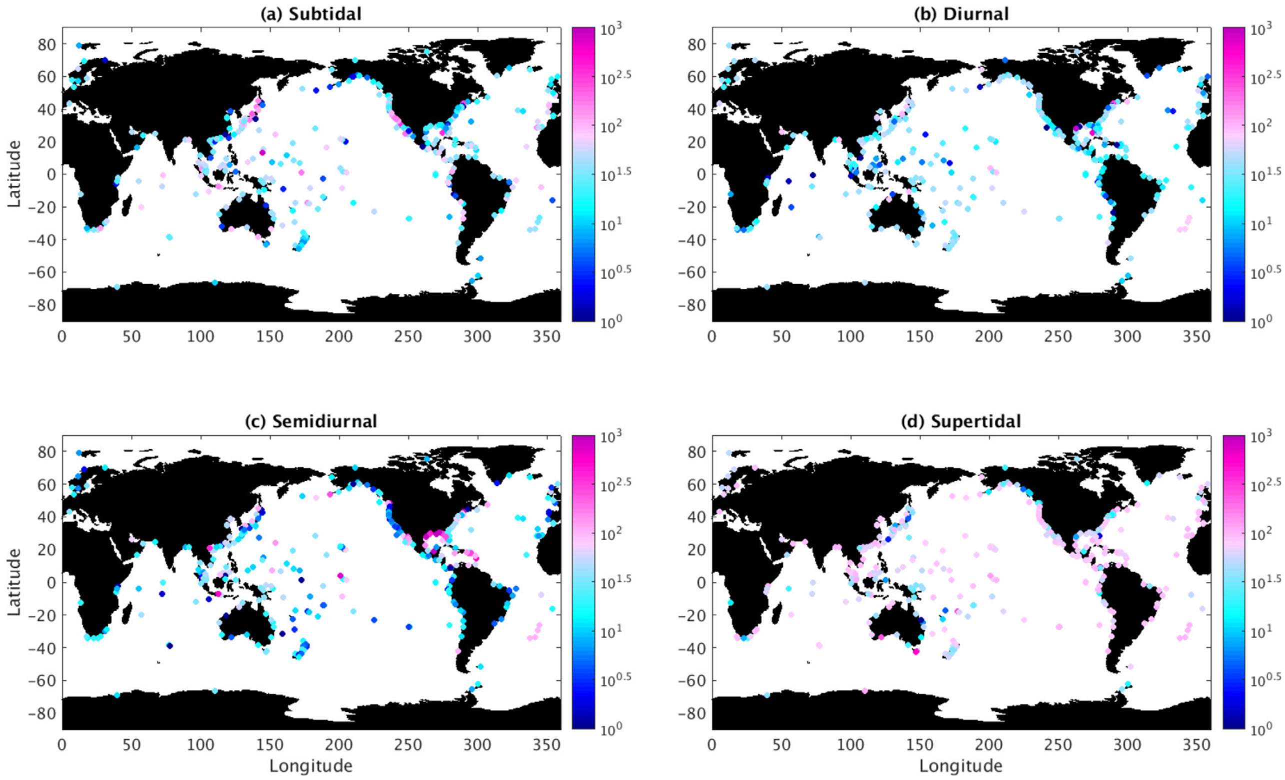

Figure 7. Percent error of HYCOM25 variance relative to tide gauge variance (see equation (5)) at each tide gauge location in (a) subtidal, (b) diurnal, (c) semidiurnal, and (d) supertidal frequency bands.

constant sections equal to 0.2. Approximately 12% of the variance is lost across the full frequency band due to the Tukey window. The frequency spectral densities are computed from each time series for each tide gauge, in situ vertical profiler, and corresponding model grid point using a discrete Fourier Transform, $\widehat{SSH}(\omega)$, given by

$$\widehat{SSH}(\omega)=\sum_{t=0}^{T-1} SSH(t)e^{-i\omega t}, \tag{2}$$

where ω denotes frequency, t denotes time, and T is the total number of samples.

The SSH variance computed over a frequency band $[\omega_{\text{min}}, \omega_{\text{max}}]$ is calculated as

$$SSH\,variance=\frac{2\delta t}{T}\int_{\omega_{\text{min}}}^{\omega_{\text{max}}} |\widehat{SSH}(\omega)|^2 d\omega, \tag{3}$$

where δt is the temporal sampling interval. We integrate over four frequency bands shown in Figure 4, the subtidal band (frequencies 1/366 cycles per day (cpd) to 0.86 cpd), the diurnal band (frequencies 0.87–1.05 cpd), the semidiurnal band (frequencies 1086–2.05 cpd), and the supertidal band (frequencies 2.06–12 cpd). In the construction of our global maps, within the diurnal and semidiurnal bands, we compute the total and nonstationary SSH variances. The nonstationary component is calculated by removing the harmonics of the five tidal constituents introduced into these HYCOM simulations via harmonic analysis [*Ray*, 1998] before spectral densities are computed. The degree of

Table 1. The Mean of SSH Variance in cm^2 Computed Over All 351 Tide Gauge Locations for Tide Gauges and Corresponding Model Grid Points in HYCOM12 and HYCOM25[a]

	Tide Gauge	HYCOM12	HYCOM25
Average total variance ($\times 10^3$)	3.2	2.9 (0.91)	3.0 (0.94)
Average subtidal variance	103.7	82.9 (0.80)	104.4 (1.01)
Average diurnal variance	402.3	336.6 (0.84)	271.1 (0.67)
Average semidiurnal variance ($\times 10^3$)	2.7	2.5 (0.93)	2.6 (0.96)
Average supertidal variance	13.1	6.3 (0.48)	4.1 (0.31)

[a]The parenthetical values are ratios of HYCOM variance to tide gauge variance.

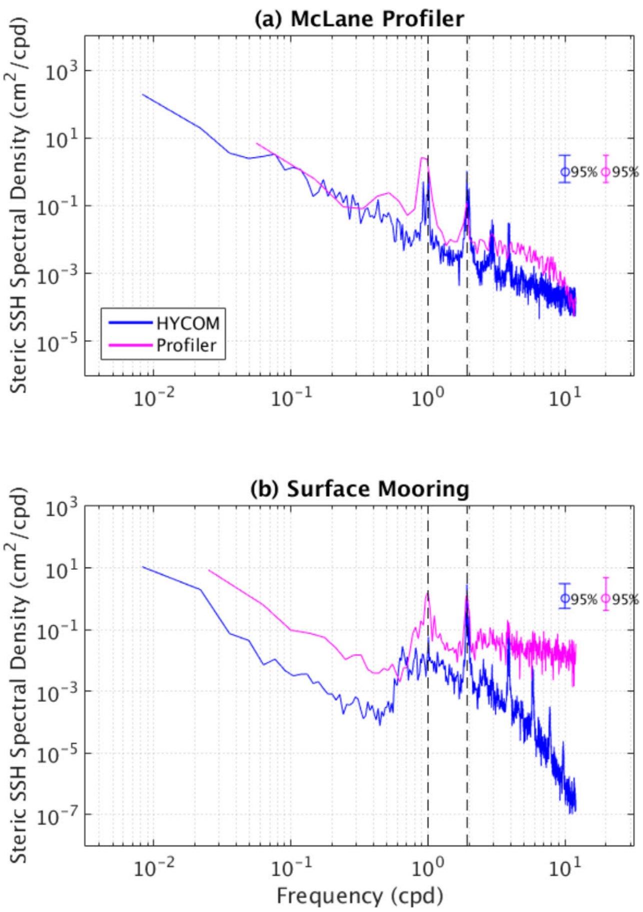

Figure 8. Example steric SSH spectral densities from (a) McLane profiler located at 120.61°E, 12.84°N, and (b) surface mooring located at 38°W, 24.58°N and corresponding HYCOM25 grid points. The dashed vertical lines denote K_1 diurnal and M_2 semidiurnal tidal frequencies. The 95% confidence intervals shown account only for random error in spectral density calculations.

nonstationarity computed here is a function of the 1 year record length of our HYCOM output. We computed nonstationary tidal signals from a 3 month time series, a 6 month time series, and a full 1 year time series at a single location near Hawai'i. We found the nonstationary signal to be 0.07% of the total tidal signal in the 3 month time series, 0.09% in the 6 month time series, and 0.17% in the full year time series. As expected and consistent with *Ansong et al*. [2015], the nonstationarity of the tidal signal increases as the record length increases. As a time saving measure, the global maps of HYCOM12 and HYCOM25 SSH variance are constructed from output subsampled at 1/4° intervals.

3. Results

3.1. Comparison to Tide Gauges

In both the model output and the tide gauge data, large peaks in SSH variance are seen at the diurnal and semidiurnal bands near 1 and 2 cpd. Figure 5 shows HYCOM/tide gauge data frequency spectral density comparisons at three example locations. The three locations are indicated on Figure 2a by filled cyan squares. Figures 5a and 5c display the comparisons at Eastport, Maine, and Lautoka, Fiji, which were chosen to represent continental and island locations, respectively, where the model performs well. The spectral densities are relatively well matched, although the model is deficient at supertidal frequencies in Figures 5a and 5b. Many of the tide gauges display a relatively flat spectrum at supertidal frequencies, which may be indicative of instrument noise or poorly resolved coastal or harbor dynamics. Figure 5b, the comparison for Puerto Armuelles, Panama, was chosen to exemplify a location with a greater model/data discrepancy. The model/data differences are particularly large between frequencies ranging from slightly less than diurnal to slightly more than semidiurnal.

The band-integrated variances in the model are reasonably well matched with the band-integrated tide gauge variances. Figure 6 shows scatterplots of the band-integrated SSH variances in the model versus tide gauge data. In the subtidal band, Figure 6a, the model shows scatter, but little to no bias. In the diurnal (Figure 6b) and semidiurnal (Figure 6c) bands, the model shows less scatter and little bias, except at low-variance values in the semidiurnal plot, where the model is biased high compared to the data. In the supertidal band, Figure 6d, the model shows scatter and a low model bias, in accordance with Figures 5a and 5b.

Discrepancies between the model and tide-gauge data could be due to a combination of factors, including inadequate model representation of complex coastal bathymetries and instrument noise at supertidal frequencies. The percent error in HYCOM25-to-tide gauge band-integrated variances is calculated as

$$Error = 100 \times \frac{|Tide\ Gauge\ Variance - HYCOM25\ Variance|}{Tide\ Gauge\ Variance}, \tag{4}$$

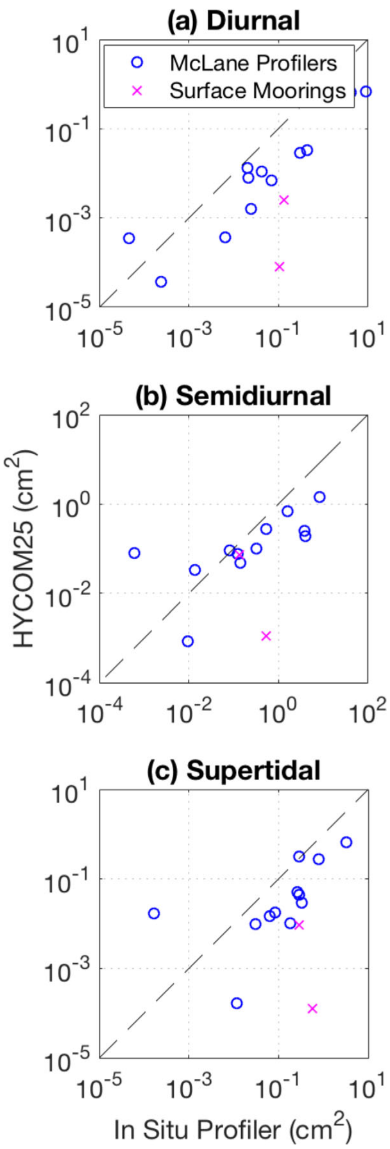

Figure 9. Scatterplots of band-integrated steric SSH variance in in situ vertical profiler data versus 1/25° HYCOM in (a) diurnal, (b) semidiurnal, and (c) supertidal frequency bands. Axis limits differ between subplots.

and is mapped in Figure 7. In the subtidal, diurnal, and semidiurnal maps, (Figures 7a–7c), the error is approximately 10% over much of the globe, with higher error near Japan in the subtidal band and in the Gulf of Mexico in the semidiurnal band. It is unclear why the model is not performing as well in the subtidal band near Japan—a highly energectic region for the subtidal flows—as in other similarly high subtidal variance regions. The supertidal band (Figure 7d) in general shows higher error across the globe, approximately 100%, in most locations. Considering Figure 7d along with Figure 6d, we see that the error seen in the supertidal map is caused by the model underestimating the supertidal variance at most locations. Again, this is consistent with what is seen in the example frequency spectral densities, Figures 5a and 5b.

The averages of the band-integrated full SSH variances, computed over the 351 tide gauge locations, from the tide gauge data and both HYCOM simulations, are given in Table 1. HYCOM25 is more closely matched to the tide gauge data in total, subtidal, and semidiurnal variance, but underestimates the variance in the diurnal and supertidal frequency bands, where HYCOM12 performs better. These rather substantial drops in variance from HYCOM12 to HYCOM25 ($\sim$20% in the diurnal band and $\sim$33% in the supertidal band) indicate that the resolution of complex bathymetries is not the primary cause of HYCOM error in these two bands; if it were, then the HYCOM25 simulations should perform better. In the supertidal band, Figure 5 show that HYCOM25 is lower than HYCOM12 in all three locations. In this band, coastal variances are in part associated with overtides [*Ray*, 2007], which can be seen clearly in Figures 5a and 5c. Again, HYCOM25 measures low compared to HYCOM12 in these overtidal peaks, suggesting HYCOM25 may have lower amplitude overtides compared to HYCOM12 globally. This may be related to the fact that the wave drag was not retuned in HYCOM25. *Ansong et al.* [2015] shows that the strength of wave drag tuning substantially affects the barotropic and internal tides in HYCOM. *Egbert et al.* [2004] and *Arbic et al.* [2008] show that even barotropic tides are impacted by the resolution of models, and that the optimal strength of wave drag in models depends on model resolution.

3.2. Comparison of Modeled Steric SSH to In Situ Estimates

Figure 8 shows example frequency spectral densities of steric SSH (equation (1)) computed from HYCOM25 compared with frequency spectral densities computed from two in situ depth-profiling instruments; one McLane profiler and one surface mooring. These example locations are indicated on the map in Figure 3a by a filled cyan square for the McLane profiler and a filled red square for the surface mooring. The example McLane profiler comparison is the best of the 12 McLane profiler comparisons and the example surface mooring profiler comparisons is the better of the two surface mooring comparisons. Large peaks are seen at tidal frequencies in both data sets as well as the model output, implying large internal tidal signals. The model matches the McLane profiler data relatively well across all frequencies, but is deficient in comparison to the surface mooring. As shown in Figure 3c, surface mooring time series were longer, allowing a HYCOM-data comparison over a wider range of frequencies. However, the McLane profilers had deeper, and much denser, vertical coverage which may contribute to a closer match between the HYCOM25 and the McLane profiler spectral density. With one exception, all the McLane profilers have measurements at depths exceeding 1000 m, while surface mooring measurements are at 350

Table 2. Globally Averaged Variance (cm^2) for Full, Steric, and Nonsteric SSH in Subtidal, Diurnal (Both Full and Nonstationary), Semidiurnal (Both Full and Nonstationary), and Supertidal Bands in HYCOM12 (H12) and HYCOM25 (H25)[a]

SSH		Subtidal	Diurnal	Diurnal (Nonstationary)	Semidiurnal	Semidiurnal (Nonstationary)	Supertidal
Full	H12	68.71	117.05	0.33	735.12	0.48	0.33
	H25	69.24	97.41	0.30	785.06	0.58	0.25
Steric	H12	34.89	0.17	0.05	0.80	0.30	0.06
	H25	34.83	0.15	0.05	1.05	0.43	0.15
Nonsteric	H12	39.63	116.96	0.30	734.79	0.31	0.31
	H25	40.00	97.34	0.27	784.59	0.32	0.16

[a]Variance was calculated over deep ocean grid points (seafloor depths greater than 1000 m).

and 120 m. Therefore, at the McLane profiler locations, the steric SSH integrations are performed over the bulk of the thermocline. Conversely, at the surface mooring locations, because the measurements do not cover all of the thermocline, errors in the representation of the thermocline in the model could create large errors in comparisons of model versus mooring frequency spectral density.

Band-integrated scatterplots of high-frequency model versus in situ steric SSH variances are given in Figure 9. Across all bands shown in Figure 9, scatter and bias are evident in the scatterplots. In the diurnal band, Figure 9a, the regression value is 0.87 and the correlation coefficient is 0.93. The semidiurnal band, Figure 9b, has a regression value of 0.71 and a correlation coefficient of 0.85. In the supertidal band, Figure 9c, the regression value is 0.79 and the correlation coefficient is 0.89. The low bias in all frequency bands apparent in Figure 9 suggests that the model is not fully resolving the internal tides or the IGW continuum. However, the regression values all exceed 0.70, suggesting that the model is resolving a nonnegligible fraction of these high-frequency motions.

3.3. Global Maps of SSH Variance

We now use the model's global coverage to our advantage. We show global maps of steric and nonsteric, computed in the model as given in Appendix A, SSH integrated over various frequency bands in HYCOM25. From the maps, we compute a spatial average of SSH variance defined as

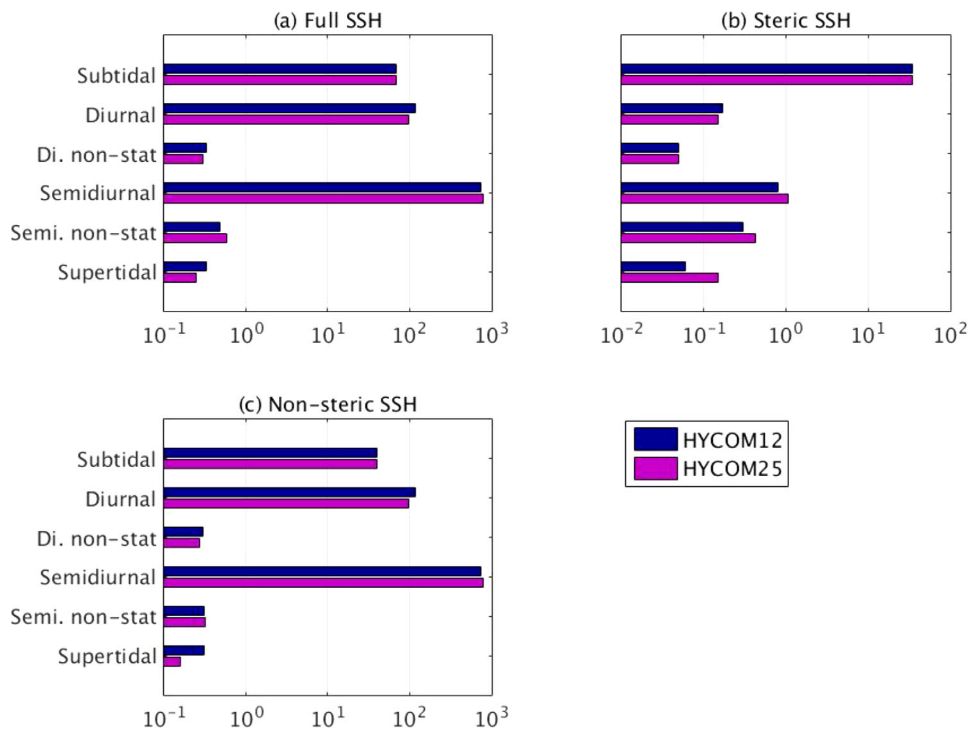

Figure 10. Bar graph of HYCOM12 and HYCOM25 variance in cm^2 in subtidal, diurnal, nonstationary diurnal, semidiurnal, nonstationary semidiurnal, and supertidal bands in (a) full, (b) steric, and (c) nonsteric SSH. Variance was calculated over deep ocean grid points (seafloor depths greater than 1000 m). Axis limits differ between subplots.

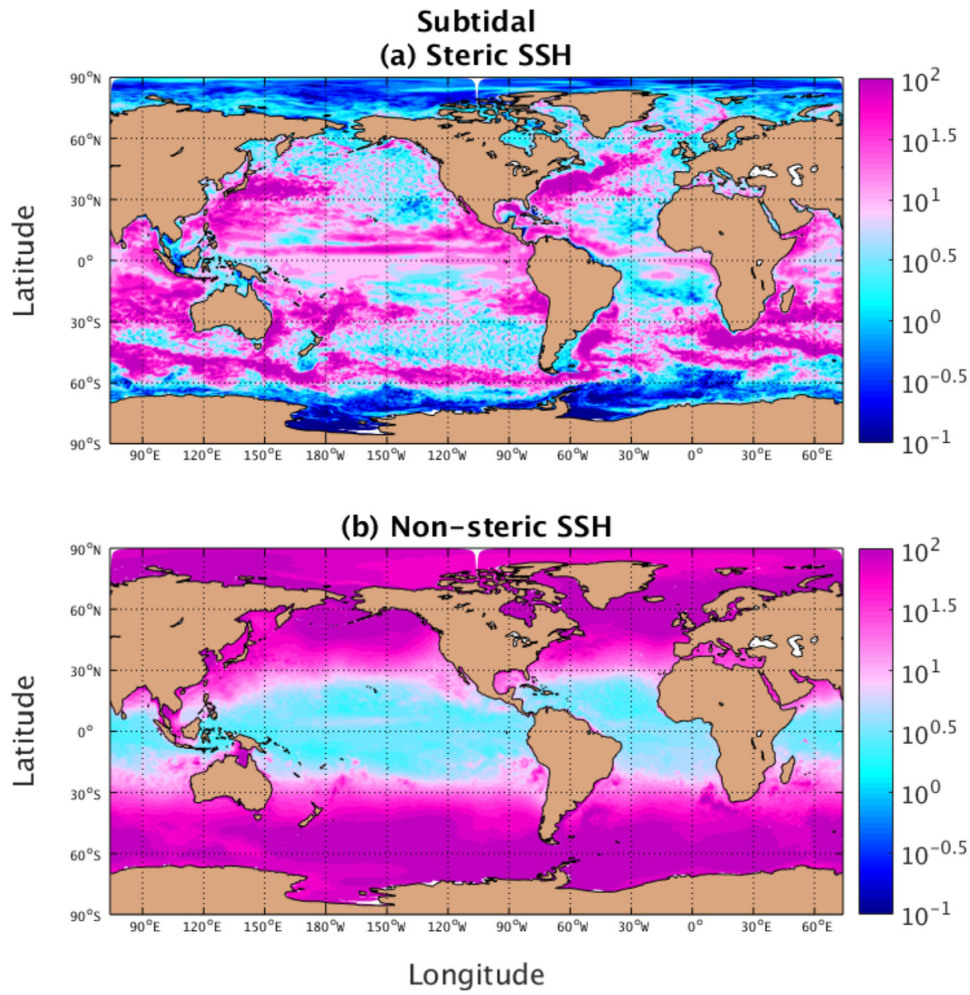

Figure 11. Global SSH variance (cm^2) from HYCOM25 in the subtidal band (frequencies 1/366 to 0.86 cpd). The 95% confidence intervals range from 96% to 104% of shown value. In this and subsequent figures, (a) steric and (b) nonsteric variances are shown.

$$\textit{Spatial Average} = \frac{\int\int \eta^2 dA}{\int\int dA}, \tag{5}$$

where η^2 is the SSH variance and dA is the area of an individual grid point. We compute the spatial average only over grid points in the deep ocean (seafloor depth $>$1000 m). The spatial average values for the full, steric and nonsteric SSH in subtidal, diurnal, semidiurnal, and supertidal bands, and for the nonstationary components of the diurnal and semidiurnal bands, are given in Table 2 and summarized visually in Figure 10, both of which will be referenced throughout the remainder of this section.

The maps of band-integrated steric and nonsteric variance in the four frequency bands, shown in Figures 11–16, exhibit features familiar from earlier studies, which will be discussed throughout this section. Note that the axis limits are not in general equal across the subplots. Figure 11 shows maps of steric and nonsteric SSH variability in subtidal frequencies. The map of subtidal steric SSH, Figure 11a, highlights strongly eddying regions, such as western boundary currents, consistent with many earlier analyses, e.g., *Ducet et al.* [2000]. The nonsteric subtidal map, Figure 11b, shows high variability in the high latitudes, due to wind and pressure forcing [*Stammer et al.*, 2000; *Tierney et al.*, 2000; *Carrère and Lyard*, 2003]. HYCOM includes the dynamic effects of atmospheric pressure as well as the static inverted barometer (IB) effect [*Ponte and Gaspar*, 1999]. Pressure- and wind-forcing drive nonsteric SSH variability over all frequency bands studied here and yield particularly strong variability at periods of 3–4 days, primarily at mid-high latitudes, where

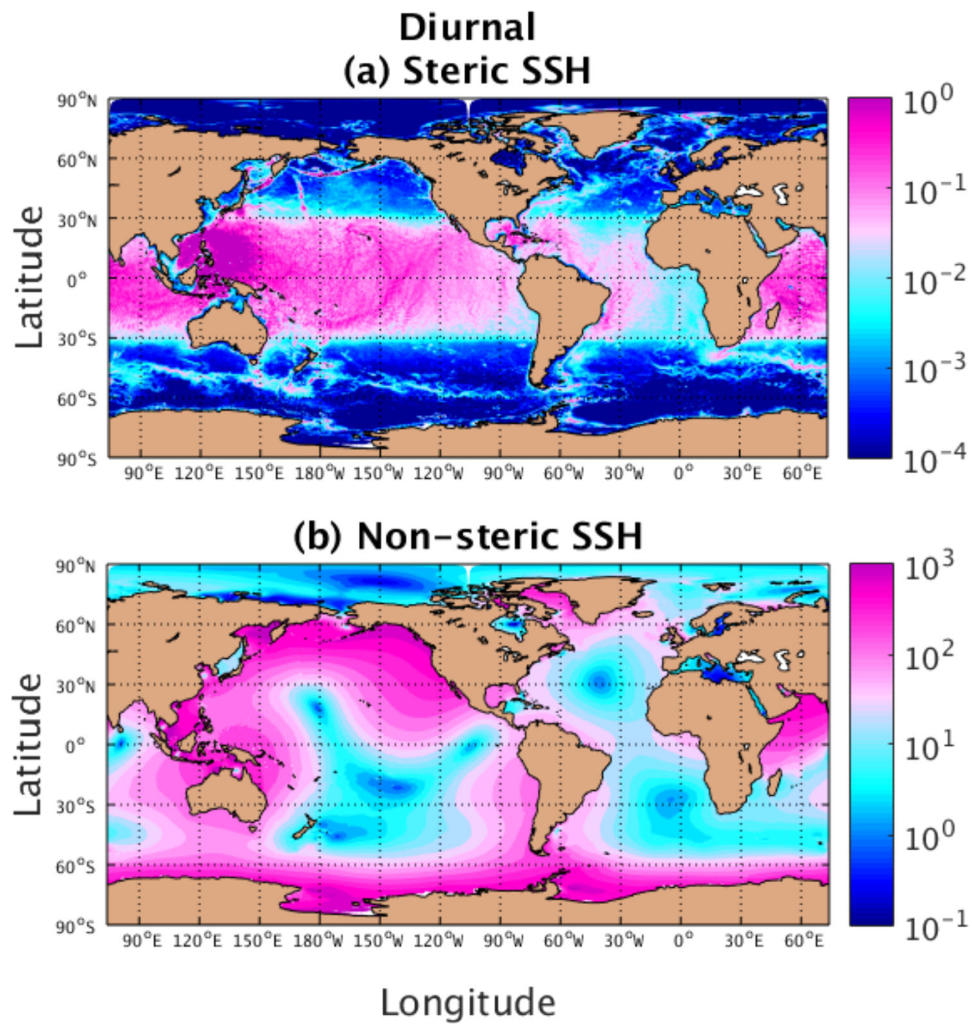

Figure 12. Global SSH variance (cm^2) from HYCOM25 in the diurnal band (frequencies 0.87–1.05 cpd). The 95% confidence intervals range from 92% to 109% of shown value.

SSH variability can be as large as 15 cm [*Fu and Chelton*, 2001]. These large variations occur primarily in the Southern Ocean where atmospheric pressure forcing is at a maximum. Our maximum HYCOM25 subtidal nonsteric SSH variance in the Southern Ocean is 22 cm. The subtidal nonsteric SSH variance is likely dominated by pressure forcing and is also strongly impacted by atmospheric wind forcing [*Carrère and Lyard*, 2003].

The nonsteric maps of the diurnal and semidiurnal bands, respectively shown in Figures 12b and 13b, show the classic barotropic tidal patterns seen in many previous studies, e.g., *Le Provost* [2001] and *Egbert et al.* [1994]. The HYCOM25 diurnal nonsteric map has a spatially averaged global variance of 97.41 cm^2 and the semidiurnal nonsteric map has a spatially averaged global variance of 785.06 cm^2 (Table 2). The HYCOM tidal variances found here are comparable with those of previous studies [*Arbic et al.*, 2004], but smaller by about 10% for unknown reasons. The five constituents used in HYCOM12 and HYCOM25 contribute 97% of the global variance found in the ten largest tidal constituents in GOT99.2 [*Ray*, 1999]. Therefore, one could expect an increase in variance of a few percent in the nonsteric and steric SSH variance estimates in both the diurnal and semidiurnal bands if more constituents were included in the HYCOM simulations. The steric diurnal and semidiurnal maps, Figures 12a and 13a, show the diurnal and semidiurnal internal tidal signals. The diurnal steric SSH, Figure 12a, does not propagate poleward of 30°, consistent with theory [*Gill*, 1982; *Shriver et al.*, 2012]. The semidiurnal steric sea level map (Figure 13a) displays a spatial distribution similar to maps of the M_2 internal tide constructed from altimeter data [*Dushaw et al.*, 2011; *Ray and Zaron*, 2016; *Zhao et al.*, 2016].

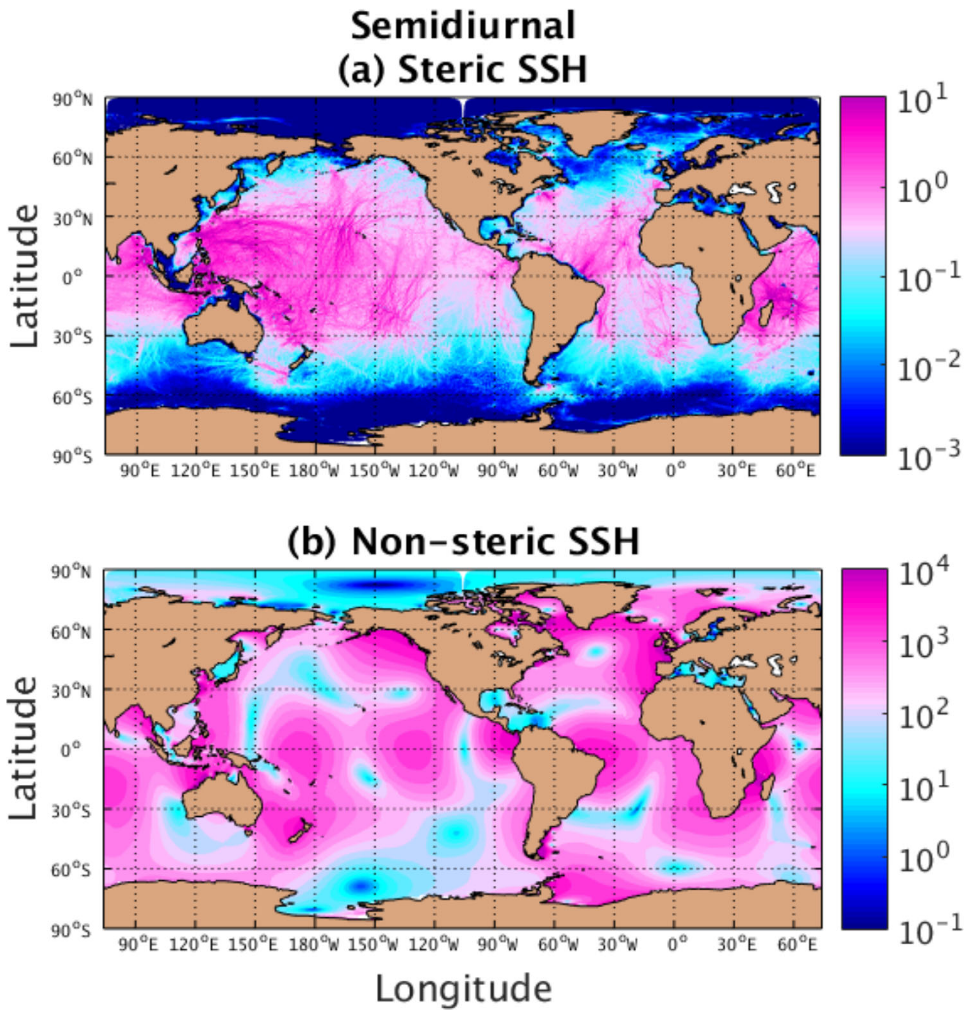

Figure 13. Global SSH variance (cm^2) from HYCOM25 in the semidiurnal band (frequencies 1.86–2.05 cpd). The 95% confidence intervals range from 92% to 109% of shown value.

The map in Figure 13a highlights regions of known large semidiurnal internal tides, for example, north of the Hawai'ian islands, near French Polynesia, and between Tasmania and Australia. In both the semidiurnal bands, the global steric SSH (internal tide) variance increases from HYCOM12 to HYCOM25 (Figure 10), indicating that model resolution is an important factor in modeling the internal tides. The global variance for the semidiurnal internal tide increases from 0.80 cm^2 in HYCOM12 to 1.05 cm^2 in HYCOM25 (Table 2), approximately equal to the $\sim$0.96 cm^2 estimated from *Zaron* [2015]. For reasons we do not understand, but which may have to do with the lack of retuning of the wave drag in HYCOM25, the globally averaged full, steric, and nonsteric SSH variances in the diurnal band decrease slightly from HYCOM12 to HYCOM25, in contrast to the results in the semidiurnal band which shows increased variance with an increased resolution. The geographies of diurnal and semidiurnal internal wave generation differ from each other [*Egbert and Ray*, 2003], implying the wave drags for the two types of motions should be tuned separately; this would be very difficult to do in present simulations.

Figures 14 and 15, respectively, show global maps of the diurnal and semidiurnal tidal band variance after the stationary part of the tide has been removed. Low-latitude and equatorial regions tend to display the largest signals in the nonstationary diurnal and semidiurnal steric (internal tide) maps [*Zaron*, 2017], and the high variance regions are correlated with the total internal tidal signals (Figures 12a and 13a). The global HYCOM25 maps of nonstationary steric SSH (internal tides) have a spatially averaged global variance of 0.05 cm^2 in the diurnal band and 0.43 cm^2 in the semidiurnal band (Table 2), the latter being comparable to

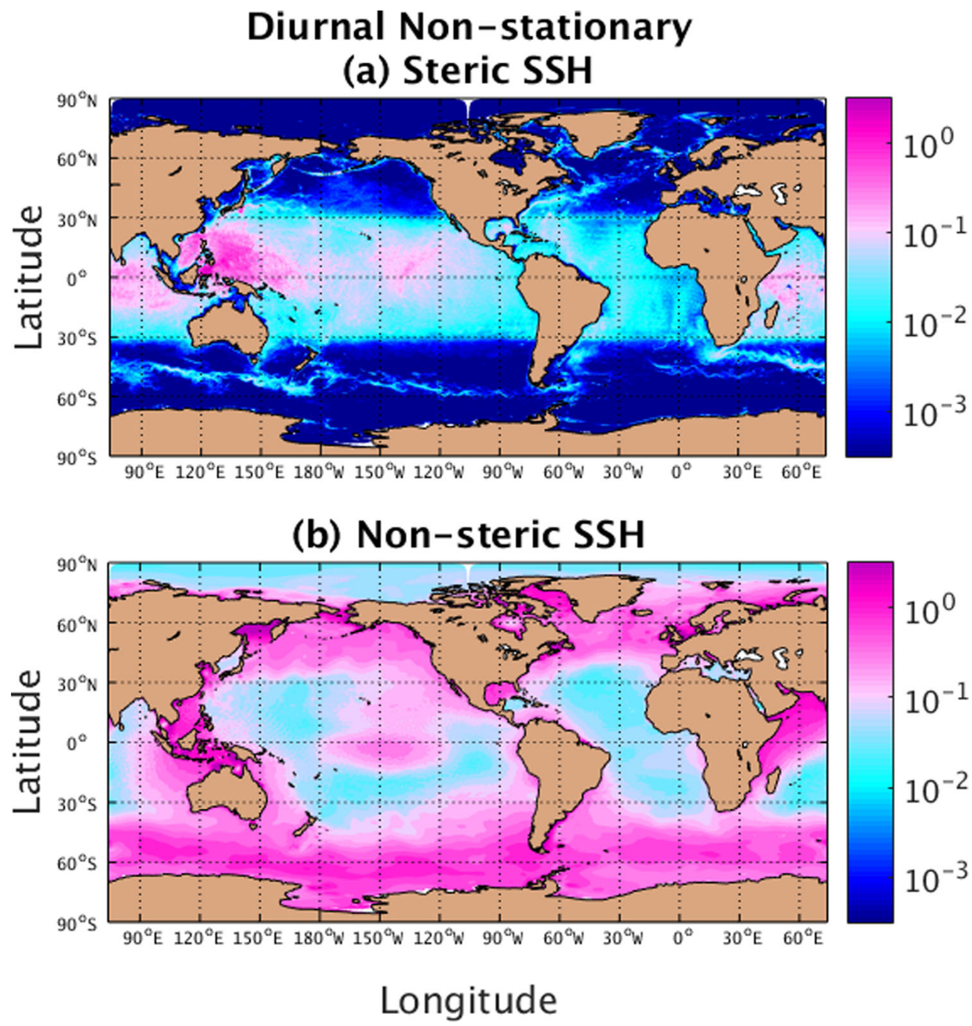

Figure 14. Global SSH variance (cm^2) from HYCOM25 in the diurnal band (frequencies 0.87–1.05 cpd) after stationary tides have been removed via harmonic analysis. The 95% confidence intervals range from 92% to 109% of shown value.

the ~0.33 cm^2 estimated from *Zaron* [2015]. HYCOM25 variance is nearly equal to HYCOM12 variance in the nonstationary diurnal band and is larger than HYCOM12 in the nonstationary semidiurnal band (Figure 10). The nonstationary component of the nonsteric semidiurnal SSH (0.32 cm^2) is smaller than the nonstationary component of the steric semidiurnal SSH (0.43 cm^2; Table 2), consistent with the idea that semidiurnal internal tide signals have a substantial nonstationary component [*Zilberman et al*., 2011]. Because the SWOT mission will be primarily focused on small horizontal scales, the small-scale, nonstationary semidiurnal steric SSH signals are of greater interest to the SWOT mission than the larger-scale nonstationary semidiurnal nonsteric SSH signals.

Maps of the supertidal variance are displayed in Figure 16. The largest nonsteric supertidal variance (Figure 16b) is along the coastlines where overtides (higher harmonics of the barotropic tide) are largest [*Ray*, 2007]. The nonsteric supertidal variance is approximately an order of magnitude smaller in the open ocean. The variance in this band is due in part to wind and atmospheric pressure forcing [*Carrère and Lyard*, 2003], and in part to overtides. The global nonsteric supertidal variance is 0.16 cm^2 in HYCOM25, less than the value in HYCOM12 (Figure 10). The drop in variance in the nonsteric supertidal band from HYCOM12 to HYCOM25 is consistent with Table 1 and is perhaps related to the low amplitudes of overtides in HYCOM25 as discussed in section 3.1.

The steric supertidal map, Figure 16a, represents a global estimate of SSH variance in the internal gravity wave continuum. As with the semidiurnal steric SSH map, the largest amplitudes are generally seen along

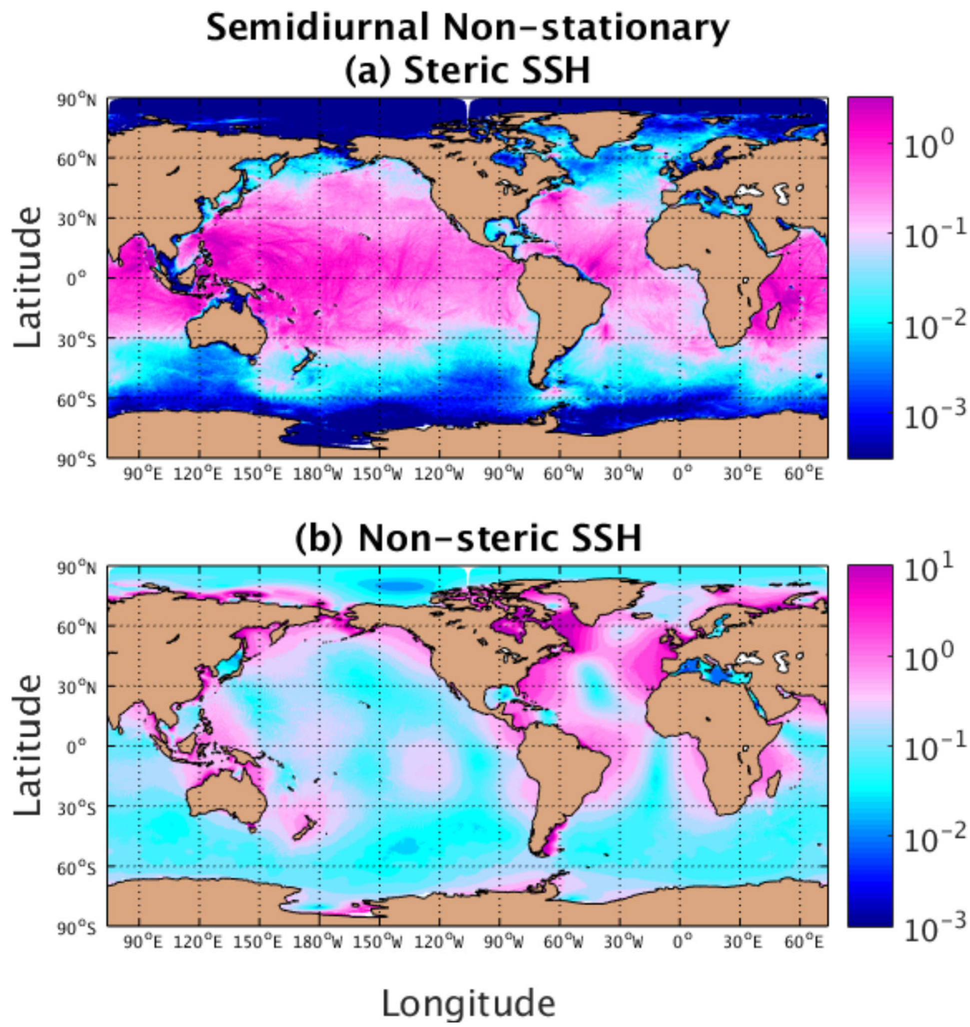

Figure 15. Global SSH variance (cm^2) from HYCOM25 in the semidiurnal band (frequencies 1.86–2.05 cpd) after stationary tides have been removed via harmonic analysis. The 95% confidence intervals range from 92% to 109% of shown value.

the equator and in low latitudes. Again, comparison of HYCOM12 and HYCOM25 in Figure 10 indicates that increasing the horizontal resolution of the model yields increased variance in the IGW continuum, consistent with results in *Müller et al*. [2015]. The global continuum variance increases from 0.06 cm^2 in HYCOM12 to 0.15 cm^2 in HYCOM25 (Table 2). The diurnal internal tidal band variance of 0.15 cm^2, the semidiurnal internal tidal band variance of 1.05 cm^2, the nonstationary internal semidiurnal tidal band variance of 0.43 cm^2, and the IGW continuum band variance of 0.15 cm^2 are measurable signals that contribute to the high frequency, and likely high wave number, variance of interest to SWOT [*Richman et al*., 2012; *Callies and Ferrari*, 2013; *Rocha et al*., 2016].

4. Summary and Discussion

Sea surface height (SSH), observable globally with satellite altimetry and tide gauge networks, is a complex mixture of many physical processes taking place over a wide range of space and time scales. Here we use a global ocean general circulation model forced by atmospheric fields and tides to map the global steric and nonsteric SSH contributions in subtidal, diurnal, semidiurnal, and supertidal frequency bands. The results complement altimeter data, which suffer from infrequent temporal sampling, and tide gauge data, which suffer from sparse spatial sampling. Comparisons with a quasi-global set of tide gauge data, a set of 14 in situ depth-profiling instrument data distributed around the globe, and previous results in the literature

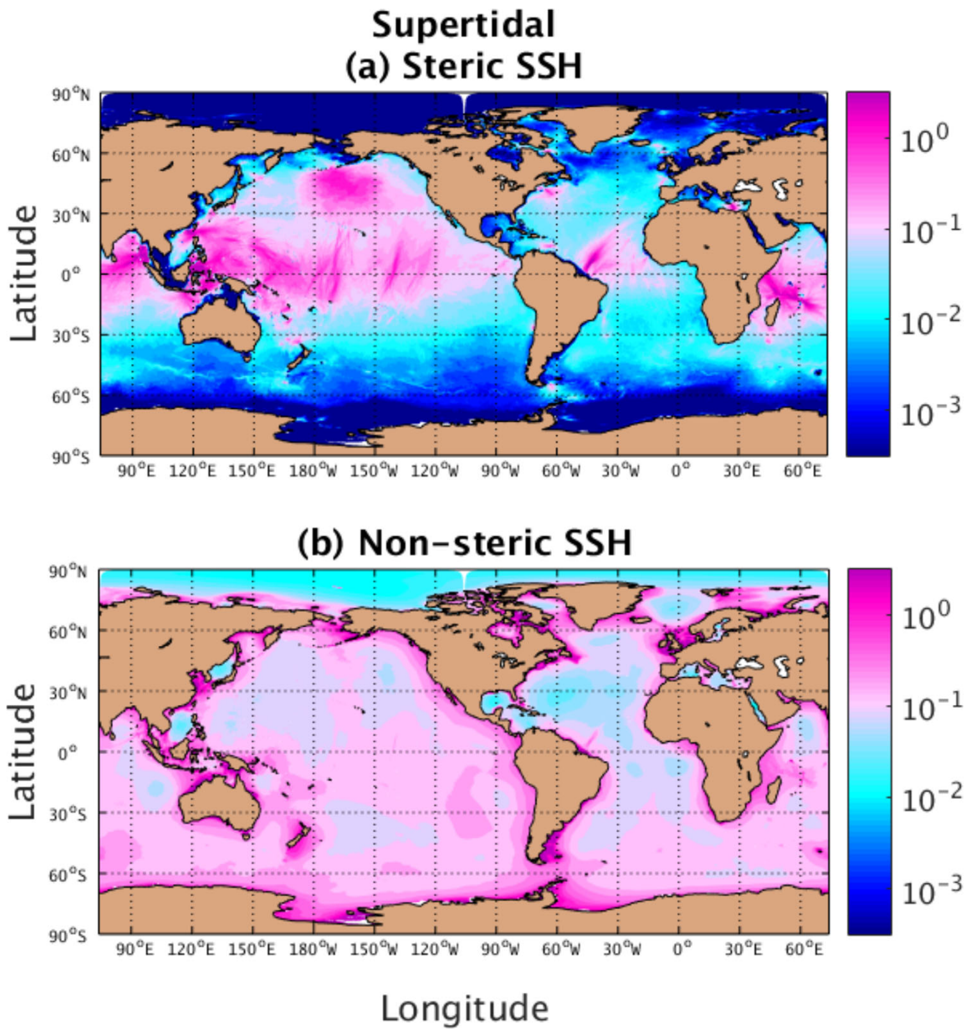

Figure 16. Global SSH variance (cm^2) from HYCOM25 in the supertidal band (frequencies 2.06–12 cpd). The 95% confidence intervals range from 98% to 101% of shown value.

indicate that the model captures well-known phenomena such as mesoscale eddies and western boundary currents (steric subtidal), the barotropic tides (nonsteric diurnal and semidiurnal), internal tides (steric diurnal and semidiurnal), and both low- and high-frequency barotropic motions driven by atmospheric pressure loading and winds (nonsteric subtidal and supertidal). The tidal and supertidal steric SSH maps produced here are of particular interest for planned future swath altimeter missions, which will focus on variability at small horizontal scales but which will alias high-frequency motions.

The semidiurnal internal tides have variances of 1.05 cm^2 (0.43 cm^2 in the nonstationary component). The nonstationary component is most prominent at low latitudes. In the supertidal band, having periods ranging from 2 to 12 hours, the steric SSH variance increases from 0.06 cm^2 in a $1/12.5^\circ$ resolution simulation to 0.15 cm^2 in a $1/25^\circ$ resolution simulation, suggesting that the model has not yet achieved numerical convergence. The supertidal steric SSH signals in the model are generally most prominent in lower latitudes. The supertidal IGW continuum variance computed over the upper ocean from the $1/25^\circ$ resolution simulation is comparable to but lower than the variance computed from in situ data, suggesting that the model estimates of the supertidal IGW continuum SSH variance may represent a lower bound. The internal tides, both phase locked and nonstationary, and the supertidal IGW continuum will appear as sources of “noise” in swath altimeter missions, and will obscure examination of low-frequency phenomena unless they can be accurately identified and removed.

Appendix A: Formulation of Steric Sea Surface Height in HYCOM

Steric sea surface height (SSH) is related to conservation of mass. We first assume local conservation of vertically integrated mass:

$$\rho_a(D+\eta_a^s)=\rho_b(D+\eta_b^s) \tag{A1}$$

where

D = rest water column thickness;

ρ_a=depth averaged density at time a;

ρ_b=depth averaged density at time b;

η_a^s=steric SSH at time a;

η_b^s=steric SSH at time b.

We rewrite equation (1) as:

$$\eta_b^s=\frac{\rho_a}{\rho_b}\eta_a^s+\frac{\rho_a-\rho_b}{\rho_b}D. \tag{A2}$$

If we define time b as our time of interest, and time a as the long-term mean, we can rewrite the standard steric SSH as

$$\eta^s=\frac{\bar{\rho}}{\rho}\overline{\eta^s}+\frac{\bar{\rho}-\rho}{\rho}D, \tag{A3}$$

where the long-term mean depth-averaged density, $\bar{\rho}$, is obtained from climatology or from a long-term mean from a prior simulation, and ρ is the instantaneous depth-averaged density. We do not have an independent way to calculate mean steric SSH, $\overline{\eta^s}$, but we do have the total (steric plus nonsteric) mean SSH, $\bar{\eta}$. Because most nonsteric components are high frequency, we assume the total mean SSH is entirely steric, i.e., $\overline{\eta^s}\approx\bar{\eta}$. HYCOM then calculates and writes out steric SSH as

$$\eta^s\approx\frac{\bar{\rho}}{\rho}\bar{\eta}+\frac{\bar{\rho}-\rho}{\rho}D. \tag{A4}$$

Acknowledgments

We thank Myrl Hendershott, Gary Mitchum, Breck Owens, and Carl Wunsch for useful discussions. We thank two anonymous reviewers for their helpful comments, which greatly improved the manuscript. The tide gauge data are supplied by the University of Hawai'i Sea Level Center and can be found at http://ilikai.soest.hawaii.edu/uhslc/data.html. M.C.B. was supported by N00014-15-1-2288. A.C.S. and B.K.A. acknowledge funding provided by Office of Naval Research grants N00014-11-1-0487 and N00014-15-1-2288, the NASA Earth and Space Science Fellowship grant NNX16AO23H, and the University of Michigan Associate Professor Support Fund, which is supported by the Margaret and Herman Sokol Faculty Awards. J.G.R., J.F.S., M.C.B., A.J.W., and L.Z. are supported by the project "Eddy resolving global ocean prediction including tides" sponsored by the Office of Naval Research. A.C.S., B.K.A., M.C.B., J.G.R., and J.F.S. acknowledge the National Aeronautics and Space Administration for providing funding under the grants NNX13AD95Q and NNX16AH79G. B.K.A. and H.S. acknowledge funding provided by National Science Foundation grant OCE-1351837. J.T.F. acknowledges funding provided by National Aeronautics and Space Administration grants NNX13AE32G, NNX16AH76G, and NNX13AE46G. This NRL contribution NRL/JA/7320-16-3156 has been approved for public release. We thank the technical teams, captains, and crews of the various vessels that deployed and recovered the in situ moorings, without whose talent and hard work the data would not be possible. Data sufficient to regenerate the figures, tables, and other results in this paper are stored on University of Michigan computers, and will be made freely available to members of the scientific community upon request.

References

Ansong, J. K., B. K. Arbic, M. C. Buijsman, J. G. Richman, J. F. Shriver, and A. J. Wallcraft (2015), Indirect evidence for substantial damping of low-mode internal tides in the open ocean, *J. Geophys. Res. Oceans*, *120*, 7997–8019, doi:10.1002/2015JC010998.

Arbic, B. K., S. T. Garner, R. W. Hallberg, and H. L. Simmons (2004), The accuracy of surface elevations in forward global barotropic and baroclinic tide models, *Deep Sea Res., Part II*, *51*, 3069–3101, doi:10.1016/j.dsr2.2004.09.014.

Arbic, B. K., J. X. Mitrovica, D. R. MacAyeal, and G. A. Milne (2008), On the factors behind large Laborador Sea tides during the last glacial cycle and the potential implications for Heinrich events, *Paleoceanography*, *23*, PA3211, doi:10.1029/2007PA001573.

Arbic, B. K., A. J. Wallcraft, and E. J. Metzger (2010), Concurrent simulation of the eddying general circulation and tides in a global ocean model, *Ocean Modell.*, *32*, 175–187, doi:10.1016/j.ocemod.2010.01.007.

Arbic, B. K., J. G. Richman, J. F. Shriver, P. G. Timko, E. J. Metzger, and A. J. Wallcraft (2012), Global modeling of internal tides within an eddying ocean general circulation model, *Oceanography*, *25*, 20–29, doi:10.5670/oceanog.2012.38.

Baker-Yeboah, S., D. R. Watts, and D. A. Byrne (2009), Measurements of sea surface height variability in the eastern Atlantic from pressure sensor-equipped inverted echo sounders: Baroclinic and barotropic components, *J. Atmos. Oceanic Technol.*, *26*, 2593–2609, doi:10.1175/2009JTECHO659.1.

Buijsman, M. C., B. K. Arbic, J. A. M. Green, R. W. Helber, J. G. Richman, J. F. Shriver, P. G. Timko, and A. J. Wallcraft (2015), Optimizing internal wave drag in a forward barotropic model with semidiurnal tides, *Ocean Modell.*, *85*, 42–55.

Buijsman, M. C., J. K. Ansong, B. K. Arbic, J. G. Richman, J. F. Shriver, P. G. Timko, A. J. Wallcraft, C. B. Whalen, and Z. Zhao (2016), Impact of parameterized internal wave drag on the semidiurnal energy balance in a global ocean circulation model, *J. Phys. Oceanogr.*, *46*, 1399–1419, doi:10.1175/JPO-D-15-0074.1.

Caldwell, P. C., M. A. Merrifield, and P. R. Thompson (2011), Sea level measured by tide gauges from the global oceans-the Joint Archive for Sea Level holdings (NCEI Accession 0019568), Version 5.5, NOAA Natl. Cent. for Environ. Inf.

Callies, J., and R. Ferrari (2013), Interpreting energy and tracer spectra of upper-ocean turbulence in the submesoscale range (1-200 km), *J. Phys. Oceanogr.*, *43*, 2456–2474, doi:10.1175/JPO-D-13-063.1.

Carrère, L., and F. Lyard (2003), Modeling the barotropic response of the global ocean to atmospheric wind and pressure forcing: Comparison with observations, *Geophys. Res. Lett.*, *30*(6), 1275, doi:10.1029/2002GL016473.

Cartwright, D. E. (1999), *Tides: A Scientific History*, 192 pp., Cambridge Univ. Press, Cambridge, U. K.

Chassignet, E. P., et al. (2009), Global ocean prediction with the HYbrid Coordinate Ocean Model (HYCOM), *Oceanography*, *22*, 64–76.

Colosi, J. A., and W. Munk (2006), Tales of the venerable Honolulu tide gauge, *J. Phys. Oceanogr.*, *36*, 967–996.

Doherty, K. W., D. E. Frye, S. P. Lberatore, and J. M. Toole (1999), A moored profiling instrument, *J. Atmos. Oceanic Technol.*, *16*, 1816–1829, doi:10.1175/1520-0426(1999)016<1816:AMPI>2.0.CO;2.

Ducet, N., P. Y. L. Traon, and G. Reverdin (2000), Global high-resolution mapping of ocean circulation from TOPEX/Poseidon and ERS-1 and −2, *J. Geophys. Res.*, *105*, 19,477–19,498, doi:10.1029/2000JC900063.

Dushaw, B. D., P. F. Worcester, and M. A. Dzieciuch (2011), On the predictability of mode-1 internal tides, *Deep Sea Res., Part 1*, *58*, 677–698, doi:10.1016/j.dsr.2011.04.002.

Egbert, G. D., and R. D. Ray (2003), Semi-diurnal and diurnal tidal dissipation from TOPEX/Poseidon altimetry, *Geophys. Res. Lett.*, *30*(17), 1907, doi:10.1029/2003GL017676.

Egbert, G. D., A. F. Bennett, and M. G. G. Foreman (1994), TOPEX/POSEIDON tides estimated using a global inverse model, *J. Geophys. Res.*, *99*, 24,821–24,852.

Egbert, G. D., R. D. Ray, and B. G. Bills (2004), Numerical modeling of the global semidiurnal tide in the present day and in the last glacial maximum, *J. Geophys. Res.*, *109*, C03003, doi:10.1029/2003JC001973.

Farrar, J. T., et al. (2015), Salinity and temperature balances at the SPURS central mooring during fall and winter, *Oceanography*, *28*, 56–65, doi:10.5670/oceanog.2015.06.

Ferrari, R., and C. Wunsch (2009), Ocean circulation kinetic energy: Resevoirs, sources, and sinks, *Annu. Rev. Fluid Mech.*, *41*, 253–282, doi:10.1146/annurev.fluid.40.111406.102139.

Fu, L. L., and A. Cazenave (Eds.) (2001), *Satellite Altimetry and Earth Sciences: A Handbook of Techniques and Applications*, Academic, San Diego, Calif.

Fu, L. L., and D. B. Chelton (2001), Large-scale ocean circulation, in *Satellite Altimetry and Earth Sciences: A Handbook of Techniques and Applications*, edited by L.-L. Fu and A. Cazanave, chap. 2, pp. 133–169, Academic, San Diego, Calif.

Fu, L. L., D. Alsdorf, R. Morrow, E. Rodriguez, and N. Mognard (Eds.) (2012), *SWOT: The Surface Water and Ocean Topography Mission: Wide-Swatch Altimetric Measurement of Water Elevation on Earth*, 228 pp., Jet Propul. Lab., Pasadena, Calif.

Garrett, C., and W. Munk (1975), Space-time scales of internal waves: A progress report, *J. Geophys. Res.*, *80*, 291–297, doi:10.1029/JC080i002p00291.

Gill, A. E. (1982), *Atmosphere-Ocean Dynamics*, Academic, San Diego, Calif.

Glazman, R. E., and B. Cheng (1999), Altimeter observations of baroclinic oceanic inertia-gravity wave turbulence, *Proc. R. Soc. A*, *455*, 90–123, doi:10.1098/rspa.1999.0304.

Hogan, T. F., et al. (2014), The navy global environemental model, *Oceanography*, *27*, 116–125, doi:10.5670/oceanog.2014.73.

Jayne, S. R., and L. C. St. Laurent (2001), Parameterizing tidal dissipation over rough topography, *Geophys. Res. Lett.*, *28*, 811–814.

Knauss, J. A. (1997), *Introduction to Physical Oceanography*, 2nd ed., Waveland Press, Long Grove, Ill.

Le Provost, C. (2001), Ocean tides, in *Satellite Altimetry and Earth Sciences*, edited by L.-L. Fu and A. Cazenave, chap. 6, pp. 267–304, Academic, San Diego, Calif.

Le Traon, P. Y., and R. Morrow (2001), Ocean currents and eddies, in *Satellite Altimetry and Earth Sciences: A Handbook of Techniques and Applications*, edited by L.-L. Fu and A. Cazanave, chap. 3, pp. 171–215, Academic, San Diego, Calif.

Metzger, E. J., O. M. Smedstad, P. J. Thoppil, H. E. Hurlburt, D. S. Franklin, G. Peggion, J. F. Shriver, and A. J. Wallcraft (2010), Validation test report for the global ocean forecast system V3.0-1/12° HYCOM/NCODA: Phase II, *NRL Memo. Rep. NRL/MR/7320-10-9236*, Stennis Space Cent., Hancock, Miss.

Müller, M., B. K. Arbic, J. G. Richman, J. F. Shriver, E. L. K. R. B. Scott, A. J. Wallcraft, and L. Zamudio (2015), Toward and internal gravity wave spectrum in global ocean models, *Geophys. Res. Lett.*, *42*, 3474–3481, doi:10.1002/2015GL063365.

Munk, W., and C. Wunsch (1998), Abysall recipes II: Energetics of tidal and wind mixing, *Deep Sea Res., Part I*, *45*, 1977–2010.

Ngodock, H. E., I. Souopgui, A. J. Wallcraft, J. G. Richman, J. F. Shriver, and B. K. Arbic (2016), On improving the accuracy of the M_2 barotropic tides embedded in a high-resolution global ocean circulation model, *Ocean Modell.*, *97*, 16–26, doi:10.1016/j.ocemod.2015.10.011.

Pattiaratchi, C. B., and E. M. S. Wijeratne (2009), Tide gauges observations of 2004-2007 Indian Ocean tsunamis from Sri Lanka and Western Australia, *Pure Appl. Geophys.*, *166*, 233–258, doi:10.1007/s00024-008-0434-5.

Ponte, R., and P. Gaspar (1999), Regional analysis of the inverted barometer effect over the global ocean using TOPEX/POSEIDON data and model results, *J. Geophys. Res.*, *104*, 15,587–15,601, doi:10.1029/1999JC900113.

Ray, R. D. (1998), Spectral analysis of highly aliased sea-level signals, *J. Geophys. Res.*, *103*, 24,991–25,003.

Ray, R. D. (1999), A global ocean tide model from TOPEX/POSEIDON altimetry: GOT99.2, *Tech. Memo. NASA/TM-1999-209478*, 58 pp., Natl. Aeronaut. and Space Admin.

Ray, R. D. (2007), Propogation of the overtide M_4 through the deep Atlantic Ocean, *Geophys. Res. Lett.*, *34*, L21602, doi:10.1029/2007GL031618.

Ray, R. D., and G. T. Mitchum (1997), Surface manifestation of internal tides in the deep ocean: Observations from altimetry and island gauges, *Prog. Oceanog.*, *40*, 135–162, doi:10.1016/S0079-6611(97)00025-6.

Ray, R. D., and E. D. Zaron (2016), M_2 internal tides and their observed wavenumber spectra from satellite altimetry, *J. Phys. Oceanogr.*, *46*, 3–22, doi:10.1175/JPO-D-15-0065.1.

Richman, J. G., B. K. Arbic, J. F. Shriver, E. J. Metzger, and A. J. Wallcraft (2012), Inferring dynamics from the wavenumber spectra of an eddying global ocean model with embedded tides, *J. Geophys. Res.*, *117*, doi:10.1029/2012JC008364.

Rocha, C. B., T. K. Chereskin, S. T. Gille, and D. Menemenlis (2016), Mesoscale to submesoscale wavenumber spectra in Drake Passage, *J. Phys. Oceanogr.*, *46*, 601–620, doi:10.1175/JPO-D-15-0087.1.

Roemmich, D., and W. B. Owens (2000), The Argo project: Observing the global ocean with profiling floats, *Oceanography*, *13*, 45–50, doi:10.5670/oceanog.2000.33.

Shriver, J. F., and H. E. Hurlburt (2000), The effect of upper ocean eddies on the non-steric contribution to the barotropic tide, *Geophys. Res. Lett.*, *27*, 2713–2716.

Shriver, J. F., B. K. Arbic, J. G. Richman, R. D. Ray, E. J. Metzger, A. J. Wallcraft, and P. G. Timko (2012), An evaluation of the barotropic and internal tides in a high resolution global ocean circulation model, *J. Geophys. Res.*, *117*, C10024, doi:10.1029/2012JC008170.

Shriver, J. F., J. G. Richman, and B. K. Arbic (2014), How stationary are the internal tides in a high-resolution global ocean circulation model?, *J. Geophys. Res. Oceans*, *119*, 2769–2787, doi:10.1002/2013JC009423.

Stammer, D., C. Wunsch, and R. M. Ponte (2000), De-aliasing of global high-frequency barotropic motions in altimeter observations, *Geophys. Res. Lett.*, *27*, 1175–1178.

Tierney, C. C., J. Whar, F. Bryan, and V. Zlotnicki (2000), Short-period oceanic circulation: Implications for satellite altimetry, *Geophys. Res. Lett*, *27*, 1255–1258.

Weller, R. A., and S. P. Anderson (1996), Surface meteorology and air-sea fluxes in the western equatorial Pacific warm pool during the TOGA Coupled Ocean-Atmosphere Response Experiment, *J. Clim.*, *9*, 1960–1990.

Wunsch, C. (1991), Global-scale surface variability from combined altimetric and tide gauge measurements, *J. Geophys. Res.*, *96*, 15,053–15,082.

Wunsch, C. (2010), Toward a midlatitude ocean frequency-wavenumber spectral density and trend determination, *J. Phys. Oceanogr.*, *40*, 2264–2281, doi:10.1175/2010JPO4376.1.

Wunsch, C., and D. Stammer (1995), The global frequency-wavenumber spectrum of oceanic variability estimated from TOPEX/POSEIDON altimetric measurements, *J. Geophys. Res.*, *100*, 24,895–24,910.

Zantopp, R. J., and K. D. Leaman (1984), The feasibility of dynamic height determination from moored temperature sensors, *J. Phys. Oceanogr.*, *14*, 1399–1406.

Zaron, E. D. (2015), Non-stationary internal tides observed using dual-satellite altimetry, *J. Phys. Oceanogr.*, *45*, 2239–2246, doi:10.1175/JPO-D-15-0020.1.

Zaron, E. D. (2017), Mapping the nonstationary internal tide with satellite altimetry, *J. Geophys. Res. Oceans*, *122*, 539–554, doi:10.1002/2016JC012487.

Zhao, Z., M. H. Alford, J. B. Girton, L. Rainville, and H. L. Simmons (2016), Global observations of open-ocean mode-1 M_2 internal tides, *J. Phys. Oceanogr.*, *46*, 1657–1684, doi:10.1175/JPO-D-15-0105.1.

Zilberman, N. V., M. A. Merrifield, G. S. Carter, D. S. Luther, M. D. Levine, and T. J. Boyd (2011), Incoherent nature of M_2 internal tides at the Hawaiian ridge, *J. Phys. Oceanogr.*, *41*, 2021–2036, doi:10.1175/JPO-D-10-05009.1.